Journal of Power Sources 201 (2012) 196–203

Contents lists available at SciVerse ScienceDirect

Journal of Power Sources

journal homepage: www.elsevier.com/locate/jpowsour

Component interactions after long-term operation of an SOFC stack with LSM cathode

J. Malzbender[a,*], P. Batfalsky[b], R. Vaßen[a], V. Shemet[a], F. Tietz[a]

[a] Forschungszentrum Jülich GmbH, IEK, 52425 Jülich, Germany
[b] Forschungszentrum Jülich GmbH, ZAT, 52425 Jülich, Germany

ARTICLE INFO

Article history:
Received 25 August 2011
Received in revised form 28 October 2011
Accepted 31 October 2011
Available online 6 November 2011

Keywords:
Solid oxide fuel cell
Degradation
Failure
Protective coating
Lanthanum strontium manganite

ABSTRACT

The reliable long-term operation of stacks with a low degradation rate is a prerequisite for the commercialization of solid oxide fuel cell (SOFC) technology. A detailed post-test analysis of stacks is of major importance in understanding degradation mechanisms. Here the results are reported of a post-test analysis of an SOFC stack with anode supported cells with Ni/YSZ anode, 8YSZ electrolyte, and a lanthanum strontium manganite (LSM) cathode operated under steady-state conditions for 19,000 h. In particular, the microstructural and chemical analyses of the relevant metallic and ceramic components are reported. The interconnects were coated with a $(Mn,Co,Fe)_3O_4$ spinel by atmospheric plasma spraying, which prevented Cr evaporating into the cathode compartment. The diffusion of Mn from the $(La,Sr)MnO_3$ cathode into the 8YSZ electrolyte led to local enrichment at grain boundaries, which might have been responsible for the degradation via electronic pathways leading to partial short-circuiting across the electrolyte. However, the ultimate failure of the stack was the result of a weakening and fracture of the 8YSZ electrolyte along grain boundaries due to the local Mn enrichment.

1. Introduction

The development of solid oxide fuel cells (SOFCs) is based on the high-temperature ionic conductivity of stabilized zirconia, which was discovered more than a century ago by Nernst [1] and integrated in SOFCs in the 1930s by Baur and Preis [2]. After considerable technological progress in recent years, SOFCs are now considered a promising alternative to convert chemical fuels directly into electrical energy [3].

There are essentially two main geometrical concepts for SOFCs: the tubular and the planar design. With respect to proof of long-term stability and demonstration of power plant technology, the tubular concept appears to be far more advanced, whereas the planar design has higher development potential and already provides higher volumetric and gravimetric power density [3]. For stationary power generation, the aim is a operating time of 80,000 h combined with an acceptable total loss of power density of 25%, resulting in an average degradation rate of 0.3%/1000 h (~2 to 3 mV kh^{-1}) [4]. Hence, degradation and lifetime are major challenges.

Typically, the cells manufactured at JÜLICH consist of an 8 mol% yttria-stabilized zirconia (8YSZ) electrolyte, a Ni and 8YSZ cermet anode and anode substrate, and a lanthanum strontium manganite (LSM) cathode. The operation temperatures are typically 800 °C for stacks with LSM cathode and 700 °C for lanthanum strontium cobalt ferrite (LSCF) cathodes [5–8]. The cells are mounted between ferritic steel interconnects [9]. The ferritic steels with high chromium content (>16%) form conductive chromia scales and are compositionally adjusted to the thermal expansion of the anode substrate [10]. Typically, Ni meshes and ceramic contact layers are used as electrical contacts on the anode and cathode side, respectively. The fuel and air compartments are separated and sealed by glass–ceramics [9].

In fact, more than 20 stacks have been operated at JÜLICH during the last four years with operation times of more than 3000 h. The use of improved steels, high-performance cells operating at lower temperatures and optimized protective layers permitted tests to be carried out for stack operation times of 34,000 h at 700 °C with an average degradation rate of 10 mV kh^{-1} at 500 mA cm^{-2} [11] and about 19,000 h at 800 °C with 4 mV kh^{-1} at 500 mA cm^{-2} (work reported here), thus coming closer to technological targets. Details on the post operational analysis of the former stack are reported in [12]. Here the results of post-test analyses of the latter SOFC stack are reported, which was shut down after the failure of one cell. In particular, the microstructural and chemical analyses of the relevant components are highlighted.

2. Experimental

The investigated stack consisted of four cells based on Ni/YSZ cermets as anode substrates with dimensions

* Corresponding author. Tel.: +49 2461616964; fax: +49 2461613699.
E-mail address: j.malzbender@fz-juelich.de (J. Malzbender).

0378-7753/$ – see front matter © 2011 Elsevier B.V. All rights reserved.
doi:10.1016/j.jpowsour.2011.10.117

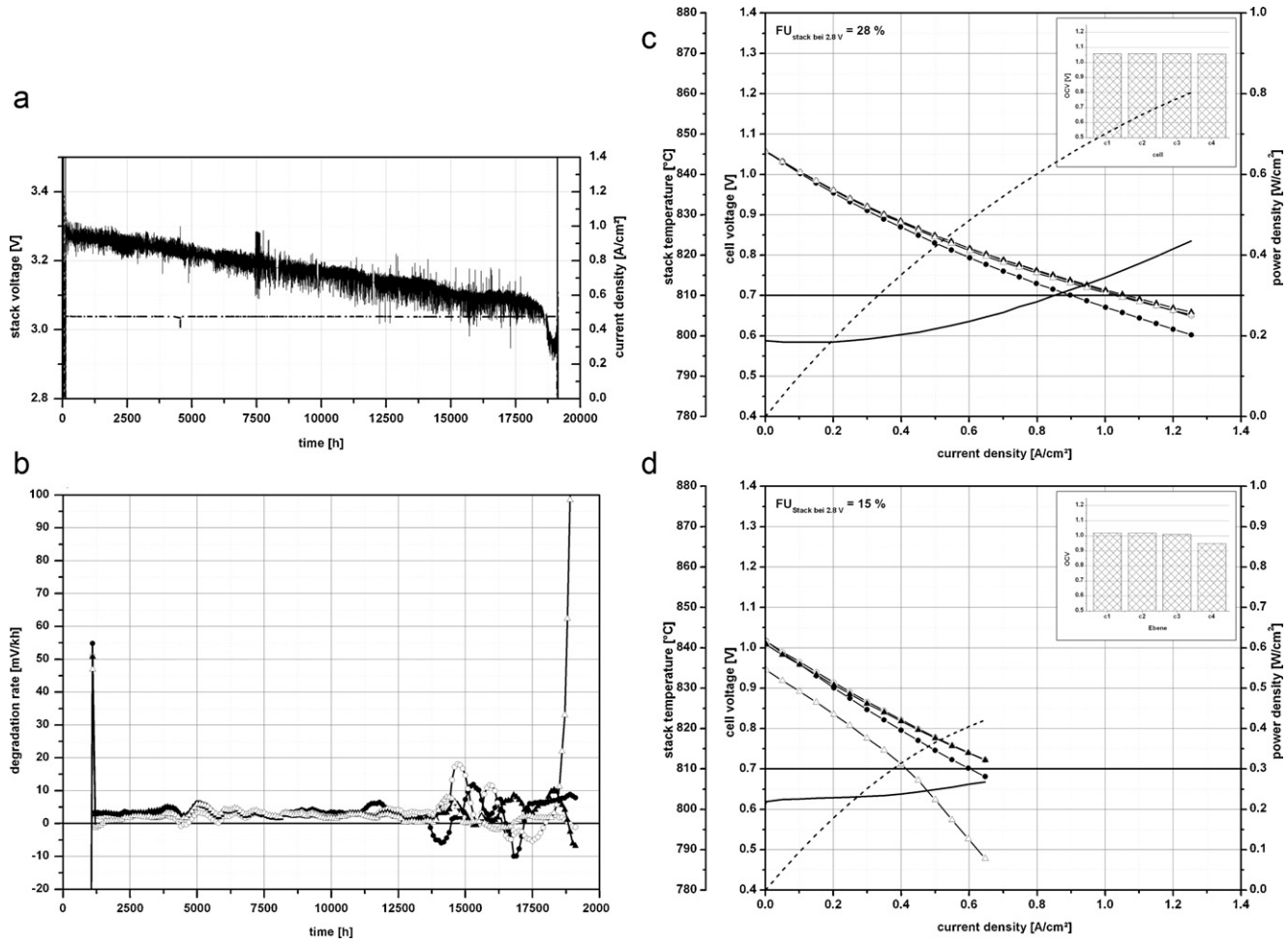

Fig. 1. (a) Time–voltage curve of the stack during long-term operation, (b) degradation curve. The stack was shut down after progressive degradation of one cell. (c and d) *I–V* measurements at the beginning and end of the stack test (800 °C; H_2, 8; H_2O, 0.75 and air, 10 l min^{-1}).

of 100 mm × 100 mm, and a double-layer cathode of LSM ($La_{0.65}Sr_{0.3}MnO_3$). The metallic parts were made of the ferritic steel Crofer22APU. The protective interconnect coating was a $MnCo_{1.9}Fe_{0.1}O_4$ spinel (MCF) with a thermal expansion coefficient adjusted to the ferritic Crofer 22 APU steel [13]. However, in contrast to previously reported stack tests [14], the coating was deposited here using atmospheric plasma spraying (APS). Such APS coatings have proven to be advantageous for the operation of SOFC stacks [15].

The coatings were deposited with a three-cathode Triplex I plasma torch (Sulzer Metco AG, Wohlen, Switzerland). The plasma gun was mounted on a six-axis robot. The plasma jet was a mixture of argon and helium gas, the total gas flow rate was Ar/He: 20/18 SLPM; current: 300 A; spraying distance: 80 mm; robot movement speed: 550 mm s^{-1} and feeding rate: 7 g min^{-1}. The spraying process used only one pass to obtain the required film thickness of about 50 μm [16]. As feedstock, an MCF powder supplied by H.C. Starck, Germany was used (grain size distribution d_{10} = 33 μm, d_{50} = 66 μm, d_{90} = 106 μm).

The ceramic contact material between cathode and protective coating was a perovskite material based on La(Mn,Cu,Co)O_3 [17]. The sealing material was a Ba–B–Ca–Al silicate glass [18]. Additional details of the stack design can be found in [19].

The stack was operated for 19,000 h at 800 °C under a steady current load of 0.5 A cm^{-2}. H_2/3% H_2O was used as fuel. The fuel utilization was 39.8%, the oxygen utilization of the air fed in was 26.6%. The four cells in the stack all showed good performance over the whole period of operation; the cell no. 1 showing about 20 mV lower voltage than the other three. Unfortunately, the test had to be stopped after a total operation time of just over 19,000 h because of a sudden loss of performance in cell no. 4. The corresponding voltage-time curves and degradation curves as well as the ASR curves at the beginning and end of the stack test are shown in Fig. 1. The post-operational analysis followed the procedure outlined in [12]. The stack was partly embedded in resin parallel to the direction of gas flow and specimens were obtained for the subsequent microstructural and chemical analysis using water jet cutting. The remaining non-embedded stack part was disassembled to permit a non-localized examination of the origin of degradation and failure.

The samples were investigated in detail using scanning electron microscopy (SEM, Ultra 55, Zeiss, Oberkochen, Germany) and energy-dispersive X-ray analysis (EDX, INCA, Oxford Instruments, Oxford, UK). X-ray diffraction (XRD) measurements were carried out with the diffractometers Siemens D5000 and Bruker-AXS/D4 Endeavor using Cu K_α radiation. Additional investigations were carried out for non-embedded specimens in order to characterize the crystalline structure of the components and layers after the stack test.

3. Results and discussion

In the following sections, the results of the stack dismantling and subsequent microstructural investigations are presented. After the macroscopic observations, the microstructural results are given

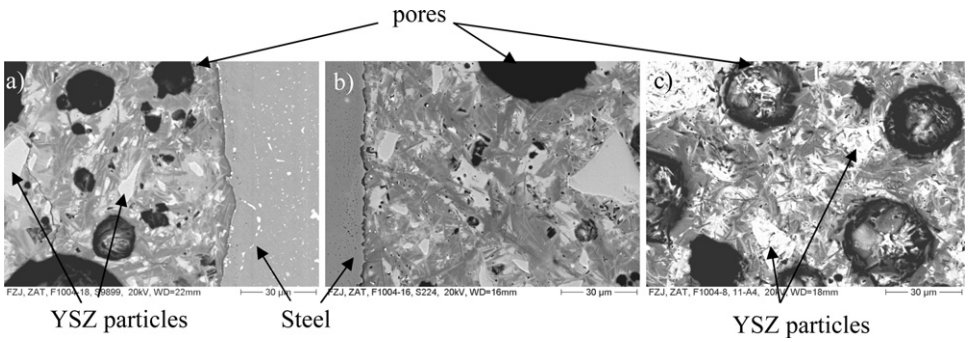

Fig. 2. Glass-ceramic sealant after stack operation times of (a) 1000 h, (b) 7000 h and (c) 19,000 h.

Table 1
Chemical composition in terms of cation ratios determined by EDX (in at.%) of points indicated in Fig. 4b.

Spectra Fig. 4b	Cr	Mn	Fe	Co	Cu	
Spectrum 1	2.0	38.4	4.7	51.1	3.8	Protective layer
Spectrum 2	0.5	38.8	4.5	51.9	4.3	Protective layer
Spectrum 4	79.5	19.2	1.3	0	0	Oxide scale
Spectrum 5	2.5	37.9	5.0	50.1	4.5	Protective layer
Spectrum 6	0	38.9	3.5	53.6	4.0	Protective layer

and discussed starting with the sealant material and then proceeding from the cathode side interconnect via the electrolyte to the anode side interconnect.

3.1. Macroscopic observations

As already mentioned above, the average degradation was reduced by a factor of two compared to stacks subjected to long-term operation at 700 °C [11] even though the stack examined here was operated at the higher temperature of 800 °C. In addition to the difference in degradation rate, one stack operated at 700 °C was shut down due to progressive degradation of all the cells, one other is still in operation at the time of writing, whereas the stack under discussion was shut down after a sudden increase in the degradation of one cell, which suggested internal failure—an aspect that received special consideration in the subsequent analysis.

The successive dissection of the non-embedded stack section after shut down revealed a color change of the uncoated metallic manifold of the cell pointing to a sudden voltage drop. According to previous experience, this color change indicated a high-temperature event, e.g. overheating due to burned fuel gas as a result of a cell leakage.

3.2. Sealant material

The sealant showed a good adherence to the interconnect with a thin reaction zone. Fig. 2 shows a comparison of the sealant material after different stack operation times (1000, 7000 and 19,000 h). It can be seen that the degree of crystallization increases with stack operation time. The phases that are visible after shorter operation times appear to increase in volume at the expense of the remaining non-crystallized glass phase. In addition, some micropores were formed after 19,000 h of stack operation due to crystallization-related shrinkage.

3.3. Protective coating and metallic interconnect (cathode side)

A low magnification optical micrograph of a polished cross-section of the cell, the adjacent contact and protection layers and the metallic interconnect is shown in Fig. 3. The MCF spinel layer showed very good adhesion to the oxide scale on the interconnect, although locally minor crack formation was observed perhaps due to the metallographic sample preparation. A well-developed, dense oxide scale formed between the protective coating and the steel interconnect. In fact, the oxidation of the steel is predominately directed inwards, in contrast to a stack with LSCF cathode and MnO_2 protective coating [12], in which the oxidation was additionally enhanced at the edges of the interconnect channels.

3.3.1. Protective coating

The MCF protective coating in the as-sprayed state is rather macroporous and the splat boundaries can be clearly seen (Fig. 4a). Due to fast cooling from the melt during the plasma spraying process, as-deposited coatings often consist of non-equilibrium phases. XRD patterns of the as-sprayed coating revealed two peaks of mixed rocksalt structure phases with different lattice parameters, the one with the smaller lattice parameter probably contains more Co. Annealing of such a coating for 19 h at 800 °C revealed the formation of $MnCo_2O_4$. The APS coatings were not heat treated after deposition, and therefore re-crystallization and densification occurs during the first thousand hours of operation [20]. Although the protective coating showed healing of splat boundaries due to the long-term operation, it also locally displayed a much lower density than in the as-sprayed condition (Fig. 4b) with an increasing microporosity gradient from the contact layer to the corrosion layer of the interconnect. A similar microstructure has been observed for coatings that were annealed for 110 h at 800 °C without current, hence it is possible to rule out a relationship to cation diffusion in the electrical field, which is known to occur in ceramic oxide

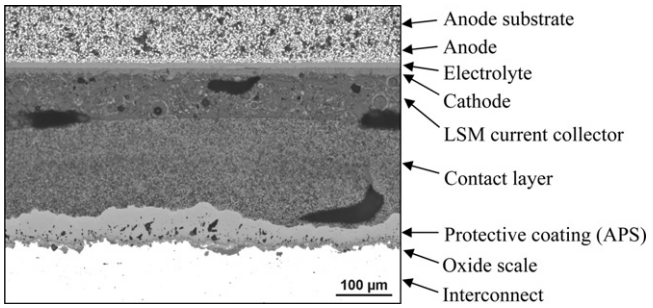

Fig. 3. Optical micrograph of a polished cross-section of the cell, the adjacent contact and protection layer and metallic interconnect.

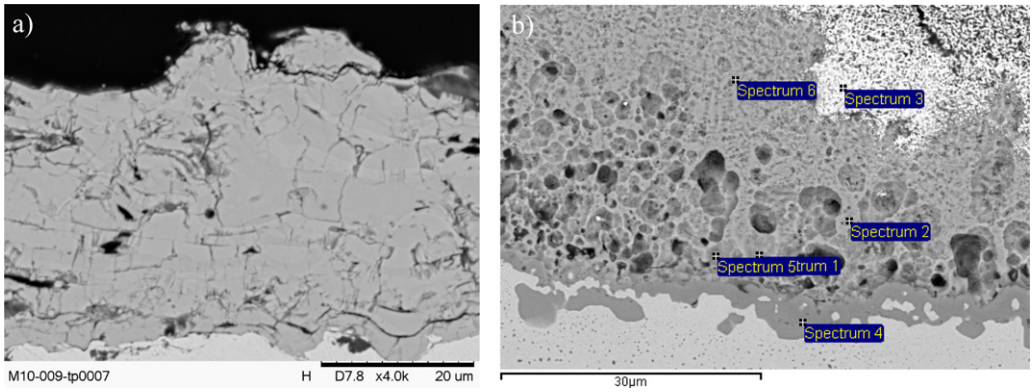

Fig. 4. (a) MCF protective coating in the as-sprayed state, (b) MCF protective coating and oxide scale after operation. The composition was verified by EDX spectra at positions 1, 2, 5 and 6.

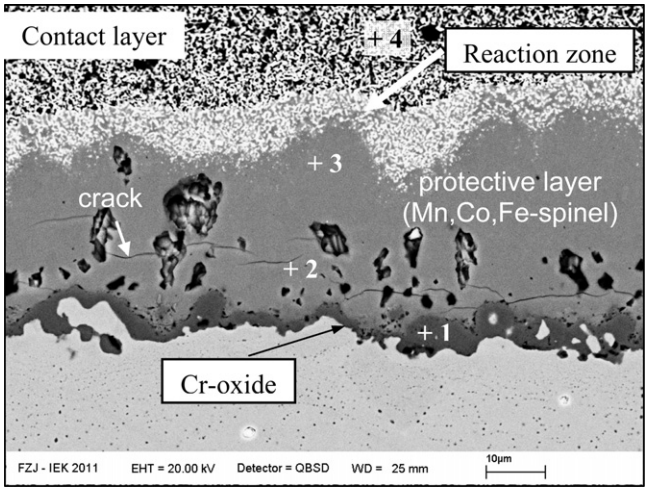

Fig. 5. SEM image of protective coating and oxide scale on interconnect after 19,000 h stack operation at 800 °C. Numbers indicate analysis areas shown in Table 2.

materials and is described as electro-transport-induced demixing [21,22], however there might be cation diffusion associated with the formation of Kirkendall voids or micropores.

An EDX analysis (Fig. 4b and Table 1) verified a very homogeneous cation distribution that can be described as $(Mn_{0.88}Cu_{0.12})(Mn_{0.27}Fe_{0.13}Co_{1.55}Cr_{0.04})O_4$ assuming AB_2O_4 spinel-type composition taking into account the required cation charge and site distribution. Compared with the initial composition, this final composition implies a decrease of Co, which is compensated by an increase of Mn and Cu as well as a small amount of Cr incorporation, mainly indicating an interaction of the APS coating with the contact layer rather than with the oxide scale layer of the Crofer 22 APU interconnect.

The SEM-based analysis of a cross-section showed no indications of reactions and hence suggests very good long-term compatibility of the protective coating with the contact layer and the metallic interconnect after long-term exposure. Although the $(Mn,Co,Fe)_3O_4$–spinel layer showed some porosity and a number of

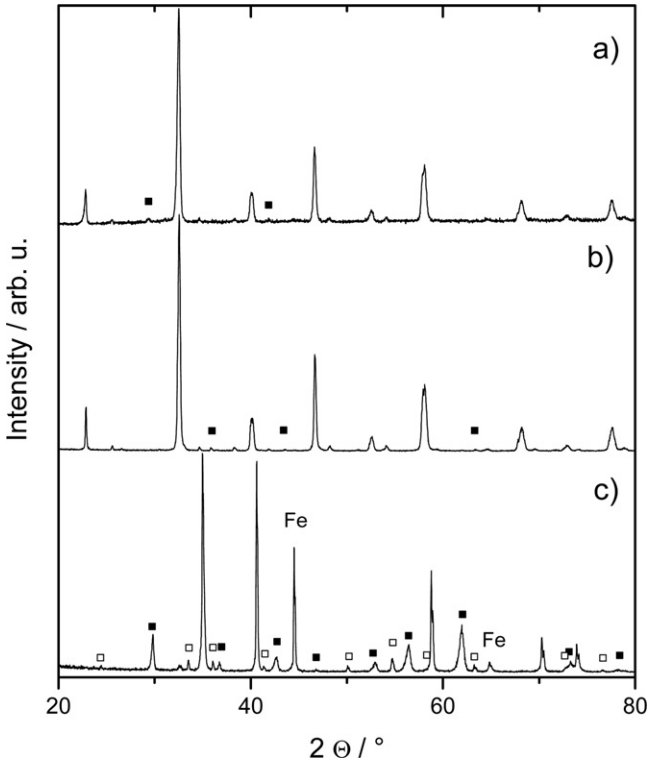

Fig. 6. XRD patterns of the contact layer in the cathode compartment (a: on the gas channels; b: on the manifold surface) and the steel surface in the anode compartment (c). The main crystallographic phase in (a) and (b) was identified as orthorhombic perovskite with $a = 5.488(4)$ Å, $b = 7.773(5)$ Å, $c = 5.528(3)$ Å and $a = 5.488(3)$ Å, $b = 7.780(6)$ Å, $c = 5.528(3)$ Å, respectively. In (a) the reflections marked with a solid square could not be identified, whereas in (b) the marked reflections belong to a spinel phase with $a = 8.303(14)$ Å. In (c) the main crystallographic phase was identified as cubic MnO with $a = 4.437(2)$ Å, the reflections marked with solid and open squares were identified as spinel with $a = 8.476(4)$ Å and Cr_2O_3, respectively.

Table 2
Chemical composition in at.-% (as determined by EDX) of the points indicated in Fig. 5.

Spectrum	O	Cr	Mn	Fe	Co	Cu	La	
1	63.2	33.4	1.7	1.6	0.1	–	–	Oxide scale
2	58.9	0.4	15.2	1.9	21.2	2.5	–	Protective layer
3	58.5	0.1	15.4	1.5	21.6	2.8	0.2	Protective layer
4	64.2	–	10.7	0.2	10.4	0.8	13.8	Contact layer

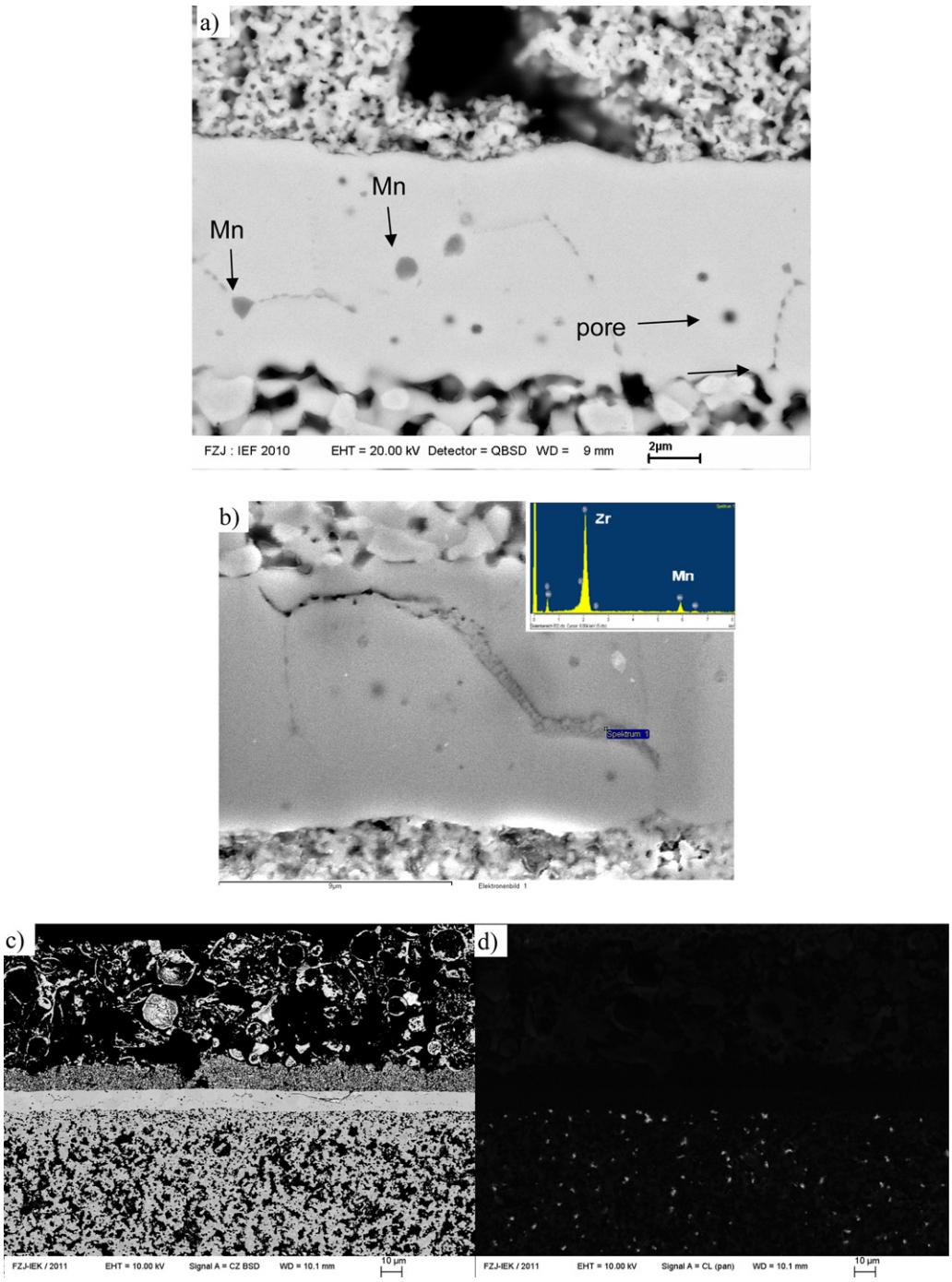

Fig. 7. The SEM images in (a) and (b) show Mn accumulation in the 8YSZ electrolyte. Whereas in (a) only an enhancement of Mn at the grain boundaries can be seen, in (b) separation already becomes visible. The EDX element analysis reveals Mn enrichment of 5–10 at.% (insert in b) along grain boundaries. Image (c) shows an area with microcracking and (d) the same area as a cathodoluminescence image verifying that monoclinic zirconia formed only in small grains in the anode.

small cracks, no spallation or delamination was observed. Beneath the protective layer the thermally grown oxide only had a thickness of ~3 μm, which is significantly smaller than the critical thickness for spallation [23].

Unlike other perovskite contact layers [24,25], the protective APS spinel coating proved to be an effective mass-transport barrier against chromium migration from the steel towards the cathode. SEM/EDX analyses (Fig. 5 and Table 2) revealed hardly any chromium at the interface between the steel oxide layer and the protective spinel layer (point 2). No chromium was detectable in the spinel layer and near its surface after 19,000 h of stack operation (point 3). Also no chromium was found in the La(Mn,Cu,Co)O_3 contact layer (Fig. 5, point 4). The APS spinel coating appears to be a very effective tool for improving the surface stability and contact resistance of the interconnect and also prevents chromia evaporation from the interconnect surface.

3.3.2. *Metallic interconnect (cathode side)*

An EDX analysis revealed that the oxide scale formed on the steel surface consisted of chromia with minor amounts of Fe and Mn (Fig. 5, point 1). Thus, during exposure the Crofer 22 APU interconnect did not form the double-layered scale consisting of

Cr_2O_3 and Cr/Mn–spinel commonly found during the oxidation of uncoated Crofer 22 APU. The excellent thermo-mechanical stability and stable electrical performance are attributed to the inhibited oxide scale growth, a good strain tolerance of the porous coating microstructure and an excellent thermal expansion match between the $(Mn,Co,Fe)_3O_4$–spinel and the metal substrate (thermal expansion coefficient RT-800 °C for Crofer 22 APU: $12.6 \times 10^{-6}\,K^{-1}$, MCF: $13.4 \times 10^{-6}\,K^{-1}$ [13]).

3.4. Contact layer and cathode

There was no significant change in the microstructure of cathode or current collector due to the long-term exposure. The composition of the contact layer after operation showed a reduction of the Cu content, probably due to loss by diffusion into the MCF layer. However, the other cation ratios remained the same as at the beginning of the stack test. Cr was not detectable in the contact layer or the cathode, which confirms the Cr retention capability of MCF already previously reported for porous coatings [26].

An XRD analysis of the contact layer at different positions revealed only small differences. As shown in Fig. 6, the XRD pattern is equivalent to an almost pure perovskite structure. The coating had the same lattice parameters on the gas channel (cell area) and on the gas manifold. The coating on the gas manifold had a small amount of spinel phase, which might be an artifact due to the underlying protective coating.

Furthermore, at the edges of the cells Sr- and Zr chromate formation was observed in the cathode close to the electrolyte interface. Since some parts of the interconnect are not coated with the protective MCF layer for technical reasons, the chromate formation can be related to evaporation of Cr from these regions.

3.5. Electrolyte

The SEM images in Fig. 7a and b show the Mn accumulation in the 8YSZ electrolyte. Whereas in Fig. 7a only an enhancement of Mn at the grain boundaries can be seen, in Fig. 7b separation of grains becomes visible. The EDX element analysis reveals a very low amount of Mn within grains (0–2 at.%), but Mn enrichment along grain boundaries of 5–10 at.% (insert in Fig. 7b). The growth of microcracks eventually resulted in large cracks (see Fig. 7c).

In fact, enriched Mn concentrations along the grain boundaries of the electrolyte material closer to the cathode interface were already noted in [27]. However, no indication of grain boundary separation was reported. The cathodes in [27] were tested at 300 mA cm^2 at 1000 °C in air for about 2000 h. Furthermore, it has been reported that 8YSZ and sub-stoichiometric LSM mixtures annealed at 950 °C for 2300 h (i.e. $La_{1-x-y}A_xMn_{1-z}Co_zO_3$ with A = Ca, Sr, $0.15 < x < 0.3$, $y = 0.05$ and $0 < z < 0.2$), typically resulted in the formation of monoclinic zirconia, whereas stoichiometric LSM materials ($y = 0$) did not show any new phases [28]. An SEM-based cathodoluminescence analysis of the 8YSZ electrolyte of the stack operated for 19,000 h did not reveal any indications of the formation of monoclinic zirconia. The monoclinic phase could only be observed as small grains in the anode structure (Fig. 7c und 7d, identical position). A similar observation was reported in [29]. The phase transformation for grains in the anode structure was correlated with the diffusion and dissolution of Ni.

The small amount of Mn found inside the electrolyte grains after the stack test agrees very well with solubility studies of transition metal cations in 8YSZ. Fig. 8 shows the solubility limit of Mn (c_{Mn}) as a function of the exposure temperature [30,31]. According to this graph, c_{Mn} is about 1 at.% at 800 °C. Therefore the higher concentrations of Mn along the grain boundaries lead to a decomposition of the cubic phase of zirconia and to increased electronic conductivity along the grain boundaries [30].

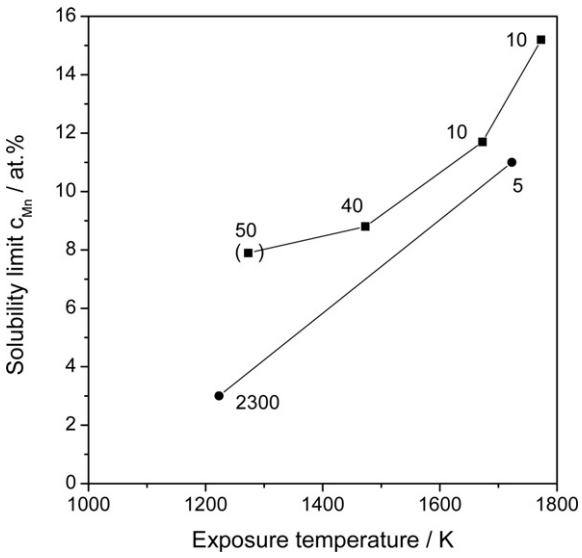

Fig. 8. Solubility limit of Mn (c_{Mn}) as a function of exposure temperature. Data were taken from Kawada et al. [30] (squares) and Tietz and Stochniol [31] (circles). The numbers at the symbols denote the duration of exposure in hours.

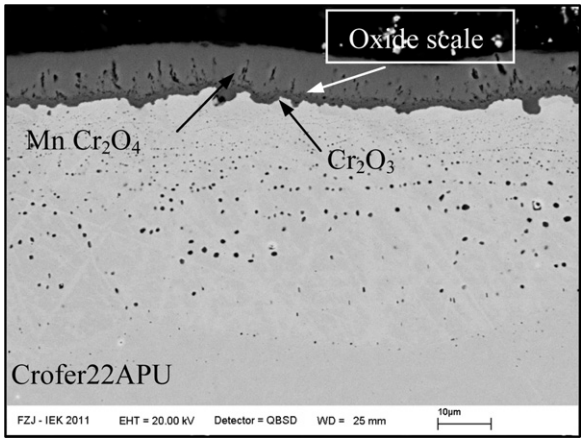

Fig. 9. Oxide scale morphology on the interconnect on the anode side after 19,000 h service at 800 °C.

An SEM analysis of electrolyte regions at the outer edges of the cell which were not coated with a cathode layer did not show any indications of Mn at the grain boundaries. This means that in the long term diffusion of manganese ions along the grain boundaries can lead to a detrimental failure of the SOFC. In contrast no such

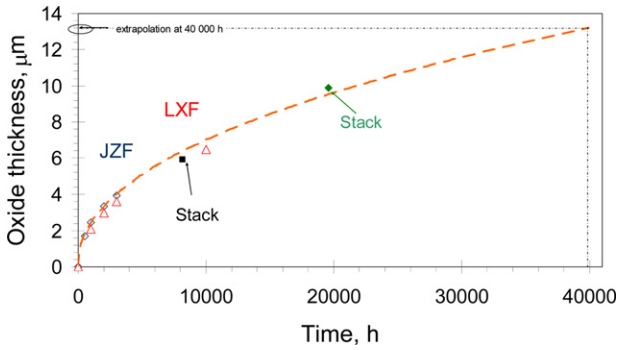

Fig. 10. Oxide scale thicknesses on different Crofer22APU batches after laboratory tests in Ar–H_2–H_2O at 800 °C [7,10] (Crofer22APU batches designated as JZF and LXF) compared with data after stack service at the anode side of the stacks.

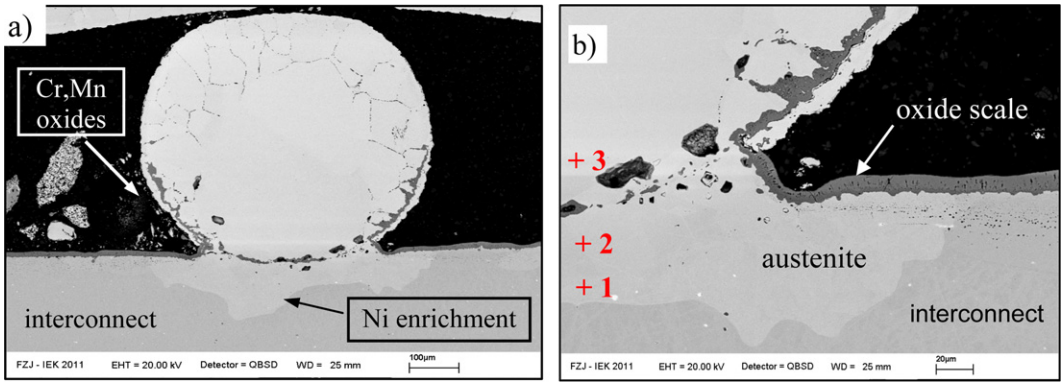

Fig. 11. (a) Electrical contact between Ni mesh and interconnect and (b) SEM cross-section of interface between Ni mesh and interconnect. Numbers indicate analysis areas shown in Table 3.

diffusion along the grain boundaries was found for Fe or Co using an LSCF cathode [11,12].

3.6. Metallic interconnect (anode side)

The interconnect surface of the manifold in the anode compartment was mainly covered by long and thin yellowish MnO crystals with NaCl-type structure as well as by spinel and chromia, the typical phases found as corrosion products of Crofer 22 APU [26].

The microstructure of the oxide scale of the uncoated interconnect (anode side) is shown in Fig. 9. The inner chromia layer was covered with a thick layer of Cr/Mn–spinel, identified by EDX analysis as $MnCr_2O_4$. The total oxide thickness was approximately 11–12 μm. It has been verified that oxide scales grown in wet hydrogen are generally thicker and rather porous, but adhere better to the metal substrate than scales grown in air [32].

Fig. 10 compares the measured oxide scale thickness on the Crofer 22 APU interconnect after stack tests with data obtained during laboratory testing in Ar/4% H_2–2% H_2O [33]. The data from laboratory and stack tests show good agreement, in spite of the substantial difference in gas composition. Assuming that oxide scale thickening obeys a classical parabolic time dependence, a thickness of approximately 14 μm for 40,000 h at 800 °C can be expected.

The interface between the Ni mesh and the interconnect is shown in Fig. 11. During stack manufacturing the Ni mesh was spot-welded to the interconnect. EDX analyses after stack operation showed that Ni diffused from the mesh into the interconnect, whereas Fe, Cr and Mn diffused from the steel into the Ni mesh (Fig. 11b and Table 3). The latter leads to the formation of Cr and Mn oxides at grain boundaries in the Ni mesh, whereas the diffusion of Ni into the ferritic steel results in the formation of austenite (Fig. 11b).

It has to be considered that the austenite has a significantly higher coefficient of thermal expansion than the other cell components ($18 \times 10^{-6}\,K^{-1}$). Additionally, the austenitization leads to a reduction of the Cr diffusion in the steel, which may result in poorer oxidation resistance [34]. An austenite layer with a width of approximately 100 μm was formed at locations where Ni and Crofer 22 APU were in direct contact (Fig. 11). It is interesting to note the SEM/EDX analyses revealed that Mn, Si, Mg and Al are enriched at the grain boundaries of the Ni mesh (Fig. 11b).

Table 3
Chemical composition in at.-% of points indicated in Fig. 9.

Spectrum	Cr	Mn	Fe	Ni
1	8.4	0.0	27.2	64.4
2	3.6	0.3	13.7	82.4
3	0.0	0.2	0.3	99.5

4. Conclusions

No significant Cr contents could be found in the cathode thus verifying that the MCF layer applied by APS is an efficient Cr barrier which can hinder the formation of strontium chromate or the formation of chromium manganese spinels at the cathode/electrolyte interface. However, Mn diffusion into 8YSZ led to local accumulation at the grain boundaries which caused probably a decrease in conductivity and a mechanical weakening and eventually separation of the grain boundaries and crack growth. The growth of these cracks eventually resulted in the fracture of one cell, burning of fuel gas and sudden failure of the stack.

The present observations indicate that degradation is due to a combination of various phenomena. If the strong effects that are usually observed due to the interaction with Cr are eliminated, other mechanisms emerge which are, however, the main challenges for the long-term operation targets of SOFC stacks. From the results, it can be concluded that the targeted operation times of SOFC stacks can become realistic by combining an LSCF cathode with an APS protective coating.

Acknowledgments

The authors gratefully acknowledge the fruitful discussions with other members of the Jülich stack dissection group, i.e. L. Blum, S.M. Gross, M. Karger, N.H. Menzler, A. Neumann and I.C. Vinke as well as L.G.J. (Bert) de Haart, H.W. Müskes and U. Packbier for the stack operation and providing the electrochemical data.

References

[1] W. Nernst, Z. Elektrochem. 6 (2) (1899) 41–43.
[2] E. Baur, H. Preis, Z. Elektrochem. 43 (1937) 727–732.
[3] L. Blum, W.A. Meulenberg, H. Nabielek, R. Steinberger-Wilckens, Int. J. Appl. Ceram. Technol. 2 (2005) 482–492.
[4] R. Steinberger-Wilckens, L. Blum, H.-P. Buchkremer, B. De Haart, J. Malzbender, M. Pap, ECS Trans. 35 (1) (2011) 53–60.
[5] R.N. Basu, G. Blass, H.-P. Buchkremer, D. Stöver, F. Tietz, E. Wessel, I.C. Vinke, J. Eur. Ceram. Soc. 25 (2005) 463–471.
[6] F. Tietz, V.A.C. Haanappel, A. Mai, J. Mertens, D. Stöver, J. Power Sources 156 (2006) 20–22.
[7] J.W. Fergus, J. Power Sources 147 (2005) 46–57.
[8] V.A.C. Haanappel, J. Mertens, D. Rutenbeck, C. Tropartz, W. Herzhof, D. Sebold, F. Tietz, J. Power Sources 141 (2005) 216–226.
[9] L. Blum, H.P. Buchkremer, R.W. Steinbrech, L.G.J. de Haart, U. Reisgen, R. Steinberger-Wilckens, Proceedings of the 8th European SOFC Forum, EFCF 2008, Lucerne, Switzerland, 2008, CD, B0306.

[10] P. Huczkowski, N. Christiansen, V. Shemet, L. Singheiser, W.J. Quadakkers, in: Mogensen (Ed.), Proceedings of the 6th European SOFC Forum, Lucerne, Switzerland, 2004, pp. 1594–1601.
[11] L.G.J. de Haart, I.C. Vinke, ECS Trans. 35 (1) (2011) 187–194.
[12] N.H. Menzler, P. Batfalsky, S.M. Groß, V. Shemet, F. Tietz, ECS Trans. 35 (1) (2011) 195–206.
[13] T. Kiefer, M. Zahid, F. Tietz, D. Stöver, H.-R. Zerfaß, in: S. Linderoth, A. Smith, N. Bonanos, A. Hagen, L. Mikkelsen, K. Kammer, D. Lybye, P.V. Hendriksen, F.W. Poulsen, M. Mogensen, W.G. Wang (Eds.), Proceedings of the 26th Risø International Symposium on Materials Science: Solid State Electrochemistry, Risø National Laboratory, Roskilde, Denmark, 2005, pp. 261–266.
[14] L.G.J. de Haart, J. Mougin, O. Posdziech, J. Kiviaho, N.H. Menzler, Fuel Cells 9 (2009) 794–804.
[15] M.J. Garcia-Vargas, M. Zahid, F. Tietz, T. Kiefer, P. Stevens, R. Vaßen, Proceedings of the 7th European SOFC Forum, European Fuel Cell Forum, 2006, CD, B081.
[16] R. Vassen, D. Hathiramani, D. Stöver, Deutsches Patent 102004 044597, Verfahren zur Herstellung dünner, dichter Keramik-schichten, 2006.
[17] F. Tietz, A. Schmidt, M. Zahid, J. Solid State Chem. 177 (2004) 745–751.
[18] S.M. Gross, D. Federmann, J. Remmel, M. Pap, J. Power Sources 196 (2011) 7338–7342.
[19] L. Blum, H.P. Buchkremer, S.M. Gross, L.G.J. de Haart, J. Quadakkers, U. Reisgen, R. Steinberger-Wilckens, R.W. Steinbrech, F. Tietz, Int. J. Appl. Ceram. Technol. 3 (6) (2006) 470–476.
[20] E. Saoutieff, G. Bertrand, M. Zahid, L. Gautier, ECS Trans. 25 (2) (2009) 1397–1402.
[21] J.-O. Hong, H.-I. Yoo, Solid State Ionics 113–115 (1998) 265–270.
[22] M. Martin, J. Chem. Thermodyn. 35 (2003) 1291–1308.
[23] W.N. Liu, X. Sun, E. Stephens, M.A. Khaleel, J. Power Sources 189 (2009) 1044–1050.
[24] K. Hilpert, D. Das, M. Miller, D.H. Peck, R. Weiß, J. Electrochem. Soc. 143 (1996) 3642–3647.
[25] Y. Larring, T. Norby, J. Electrochem. Soc. 147 (2000) 3251–3256.
[26] R. Trebbels, T. Markus, L. Singheiser, J. Electrochem. Soc. 157 (2010) B490–B495.
[27] M.J. Jorgensen, P. Holtappels, C.C. Appel, J. Appl. Electrochem. 30 (2000) 411–418.
[28] F. Tietz, G. Stochniol, in: P. Otschik (Ed.), Proceedings of the DKG/DGM-Symposium, Werkstoff-Informationsgesellschaft mbH, Frankfurt, Germany, 1997, pp. 229–242.
[29] H. Kishimoto, T. Shimonosono, K. Yamaji, M.E. Brito, T. Horita, H. Yokokawa, ECS Trans. 35 (2011) 1171–1176.
[30] T. Kawada, N. Sakai, H. Yokokawa, M. Dokiya, Solid State Ionics 53–56 (1992) 418–425.
[31] F. Tietz, G. Stochniol, unpublished results, 1997.
[32] W.J. Quadakkers, J. Piron Abelan, V. Shemet, L. Singheiser, Mater. High Temp. 20 (2003) 115–127.
[33] V. Shemet, P.O. Santacreu, W.J. Quadakkers, L. Singheiser, ASME 7th International Fuel Cell Science Engineering & Technology Conference, June 8–10, Newport Beach, CA, USA, 2009, ISBN 978-0-7918-4881-4, pp. 913–915.
[34] J. Pirón Abellán, W.J. Quadakkers, Berichte des Forschungszentrums Jülich Report No. JUEL-4170, 2005.